INTERNATIONAL JOURNAL FOR NUMERICAL METHODS IN FLUIDS, VOL. 13, 713–737 (1991)

A SPECTRAL COLLOCATION METHOD FOR COMPRESSIBLE, NON-SIMILAR BOUNDARY LAYERS

C. DAVID PRUETT AND CRAIG L. STREETT

Theoretical Flow Physics Branch, Mail Stop 156, NASA Langley Research Center, Hampton, Virginia 23665, U.S.A.

SUMMARY

An efficient and highly accurate algorithm based on a spectral collocation method is developed for numerical solution of the compressible, two-dimensional and axisymmetric boundary layer equations. The numerical method incorporates a fifth-order, fully implicit marching scheme in the streamwise (timelike) dimension and a spectral collocation method based on Chebyshev polynomial expansions in the wall-normal (spacelike) dimension. The discrete governing equations are cast in residual form and the residuals are minimized at each marching step by a preconditioned Richardson iteration scheme which fully couples energy, momentum and continuity equations. Preconditioning on the basis of the finite difference analogues of the governing equations results in a computationally efficient iteration with acceptable convergence properties. A practical application of the algorithm arises in the area of compressible linear stability theory, in the investigation of the effects of transverse curvature on the stability of flows over axisymmetric bodies. The spectral collocation algorithm is used to derive the non-similar mean velocity and temperature profiles in the boundary layer of a 'fuselage' (cylinder) in a high-speed (Mach 5) flow parallel to its axis. The stability of the flow is shown to be sensitive to the gradual streamwise evolution of the mean flow and it is concluded that the effects of transverse curvature on stability should not be ignored routinely.

KEY WORDS Spectral collocation methods Compressible flow Boundary layer equations Stability theory Transverse curvature

INTRODUCTION

In modern aerodynamics the boundary layer approximation is an invaluable tool of widespread applicability. Although it is still beyond the capability of the present generation of supercomputers to solve the compressible Navier–Stokes equations for complete aerodynamic configurations, it is commonplace for engineering purposes to patch inviscid 'outer' solutions to the Euler equations with 'inner' solutions to the boundary layer equations to obtain realistic lift and drag estimates. A different application, and the motivation for this work, lies in the area of stability and transition, for which solutions to the boundary layer equations provide the 'mean flow' velocity and temperature profiles of stability analyses. In this latter context, accuracy is very important, particularly for high-speed flows whose stability can exhibit extreme sensitivity to variations in the mean, as will be shown.

In general, the differential equations which describe two-dimensional or axisymmetric boundary layers define initial boundary value problems (IBVP) in which the streamwise spatial coordinate is timelike. For a limited subclass of problems, similarity solutions exist, in which case the timelike variation vanishes. Our interest here is in the more general case of spatially evolving boundary layers.

0271–2091/91/160713–25$12.50

Received September 1990
Revised November 1990

The papers of Blottner,[1,2] Harris and Blanchard[3] and Wornom[4] provide a thorough review of the state of the art in computational methods for two-dimensional and axisymmetric boundary layers prior to 1982. In the timelike direction, implicit marching techniques are used almost universally. Fully explicit methods for the boundary layer equations have not met with success in practice owing to their peculiar nature. Finite difference methods dominate among techniques for discretization of the spacelike variable. Blottner[1,2] examines a number of second-order-accurate finite difference methods appropriate to the numerical computation of incompressible and compressible boundary layer flows. Harris and Blanchard[3] incorporate second-order methods into a versatile computer code which is capable of computing compressible laminar, transitional or turbulent boundary layers for a wide class of geometries and flow conditions. Wornom[4] compares higher-order methods and presents a fourth-order box scheme which remains a standard of efficiency and accuracy among finite difference methods for incompressible laminar boundary layers. Very recently, spectral numerical methods have been adapted to the incompressible boundary layer equations by Streett *et al.*[5] Spectral techniques are advantageous in that one obtains a high degree of accuracy relative to finite difference methods with far fewer grid points or, from a different perspective, higher accuracy is obtained with an equivalent number of points. To date, the compressible boundary layer equations have been treated exclusively by finite difference methods.

In this paper we adapt the spectral collocation method of Streett *et al.*[5] to the compressible boundary layer equations and demonstrate the method in computing the non-similar boundary layer of a cylinder in a high-speed flow parallel to its axis. The numerical method incorporates a high-order, fully implicit, finite difference technique in the marching direction and a spectral collocation technique based on Chebyshev polynomials in the wall-normal direction. The spectrally accurate, discrete governing equations are cast in residual form and the residuals are minimized at each marching step by a preconditioned Richardson iteration[6] scheme which fully couples energy, momentum and continuity equations. Construction of the preconditioner based on finite difference analogues of the discrete governing equations leads to a computationally efficient iteration with acceptable convergence properties.

The next section discusses the compressible boundary layer equations and the particular scalings and transformations used for the model (cylindrical) geometry. The numerical method is presented in detail in the third section. In the fourth section the spectral method is used to derive the boundary layer velocity and temperature profiles along a cylindrical 'fuselage' in high-speed flow, and the spectrally obtained results are validated against those obtained by a well-proven finite difference code. The linear stability of the flow along the cylinder is then examined to assess the sensitivity of certain primary instability mechanisms to the effects of transverse curvature, including streamwise variations in the mean flow. The final section closes with concluding remarks regarding the numerical method and some implications of this work for compressible linear stability theory.

GOVERNING EQUATIONS AND SCALING

Consider the compressible flow along an axisymmetric body at zero incidence angle and of radius $\bar{R}(\bar{x})$, where $\bar{x}$ is the arc length along the body measured from the stagnation point, $\bar{y}$ is the wall-normal co-ordinate and $\bar{r}$ is the radial co-ordinate from the axis of revolution, as shown in Figure 1. If $\bar{u}$ and $\bar{v}$ denote the velocity components in the $\bar{x}$- and $\bar{y}$-direction respectively, then the evolution of the laminar boundary layer along the body is defined by equations (1).[2,7] The remaining variables $\bar{T}$, $\bar{p}$, $\bar{\rho}$, $\bar{\mu}$ and $\bar{\kappa}$ are respectively the temperature, pressure, density, viscosity

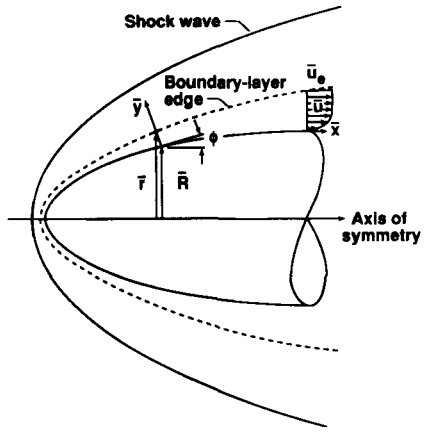

Figure 1. Co-ordinate system and notation for the boundary layer on an axisymmetric body

and thermal conductivity, and $\bar{C}_p$ is the specific heat at constant pressure, assumed here to be constant.

$$\bar{\rho}\bar{C}_p\bar{u}\frac{\partial\bar{T}}{\partial\bar{x}}+\bar{\rho}\bar{C}_p\bar{v}\frac{\partial\bar{T}}{\partial\bar{y}}=\bar{u}\frac{\partial\bar{p}}{\partial\bar{x}}+\frac{1}{\bar{r}}\frac{\partial}{\partial\bar{y}}\left(\bar{r}\bar{\kappa}\frac{\partial\bar{T}}{\partial\bar{y}}\right)+\bar{\mu}\left(\frac{\partial\bar{u}}{\partial\bar{y}}\right)^2, \tag{1a}$$

$$\bar{\rho}\bar{u}\frac{\partial\bar{u}}{\partial\bar{x}}+\bar{\rho}\bar{v}\frac{\partial\bar{u}}{\partial\bar{y}}=-\frac{\partial\bar{p}}{\partial\bar{x}}+\frac{1}{\bar{r}}\frac{\partial}{\partial\bar{y}}\left(\bar{r}\bar{\mu}\frac{\partial\bar{u}}{\partial\bar{y}}\right), \tag{1b}$$

$$\frac{\partial}{\partial\bar{x}}(\bar{r}\bar{\rho}\bar{u})+\frac{\partial}{\partial\bar{y}}(\bar{r}\bar{\rho}\bar{v})=0. \tag{1c}$$

Equations (1a–c) are derived from the steady, compressible Navier–Stokes equations under the classical boundary layer assumptions $\bar{u}>\bar{v}$ and $\partial/\partial\bar{y}>\partial/\partial\bar{x}$ and describe respectively the conservation of energy, streamwise momentum and mass.[8] The momentum equation in the azimuthal direction vanishes owing to the assumption of axisymmetry and the conservation law of momentum in the wall-normal direction degenerates to

$$\partial\bar{p}/\partial\bar{y}=0, \tag{1d}$$

which states that pressure is constant across the boundary layer.

System (1) is closed by the specification of an equation of state, a viscosity law $\bar{\mu}(\bar{T})$ and a conductivity law $\bar{\kappa}(\bar{T})$. As the equation of state we take the ideal gas law

$$\bar{p}=\bar{\rho}\bar{R}_g\bar{T}, \tag{1e}$$

where $\bar{R}_g$ is the ideal gas constant. Equation (1e) is valid for a thermally perfect gas, which limits its practical application to edge Mach numbers less than about 6.[8] We adopt the Sutherland law[8] to model viscosity–temperature and conductivity–temperature relations. These will be defined precisely once variables have been made dimensionless.

Non-dimensionalization

To simplify the presentation of the method, we consider only laminar flow and assume constant post-shock edge conditions, which we denote by subscript 'e'. Moreover, for expository purposes

we restrict consideration to the simplest axisymmetric body, the cylinder, in the absence of a streamwise pressure gradient ($\partial\bar{p}/\partial\bar{x}=0$). However, we note that equations (1) are quite general in the sense that they model the boundary layer along a cylinder, a sharp cone, a blunt cone or a generic axisymmetric shape, depending on the definition of the geometry function $\bar{R}(\bar{x})$. In general,

$$\bar{r}(\bar{x},\bar{y})=\bar{R}(\bar{x})+\bar{y}\cos\phi(\bar{x}), \tag{2a}$$

where ϕ is the angle of the surface tangent relative to the axis of symmetry. Specifically, (2a) reduces to (2b) for the cylinder,

$$\bar{r}=\bar{R}+\bar{y}, \tag{2b}$$

where $\bar{R}$ is the (constant) radius, and to (2c) for the sharp cone,

$$\bar{r}=\bar{x}\sin\phi+\bar{y}\cos\phi, \tag{2c}$$

where ϕ is the cone half-angle. Moreover, if $\bar{r}=1$, system (1) degenerates to the boundary layer equations for flat plate flow. Furthermore, by clever co-ordinate transformation (see Reference 9, for example) it is possible to adapt equations (1) to spatially varying edge conditions; and by reinterpretation of the viscosity,[3] turbulent and transitional boundary layers are modelled by (1). The reader is referred to these sources for adaptation of the method to other specific applications.

For the cylindrical geometry shown in Figure 2 and defined by (2b) we prefer the scaling of Duck[10] to conventional boundary layer scaling to render equations (1) dimensionless:

$$x=(1/Re)\,\bar{x}/\bar{R}, \qquad y=\bar{y}/\bar{R}, \qquad r=\bar{r}/\bar{R}, \tag{3a}$$

$$u=\bar{u}/\bar{u}_e, \qquad \tilde{v}=Re\,\bar{v}/\bar{u}_e, \tag{3b}$$

$$p=\bar{p}/\bar{\rho}\bar{u}_e^2, \qquad \rho=\bar{\rho}/\bar{\rho}_e, \qquad \theta=\bar{T}/\bar{T}_e, \tag{3c}$$

$$\mu=\bar{\mu}/\bar{\mu}_e, \qquad \kappa=\bar{\kappa}/\bar{\kappa}_e. \tag{3d}$$

In (3) the Reynolds number is defined on the basis of radius $\bar{R}$ and edge conditions, i.e.

$$Re=\bar{\rho}_e\bar{u}_e\bar{R}/\bar{\mu}_e. \tag{4}$$

Duck's scaling for the cylinder has the advantage over conventional scaling in that the dimensionless governing equations (5) are completely independent of Re; consequently, solutions to (5) are universal with respect to Re.

$$\rho u\frac{\partial\theta}{\partial x}+\rho\tilde{v}\frac{\partial\theta}{\partial y}=\frac{1}{rPr}\frac{\partial}{\partial y}\left(r\kappa\frac{\partial\theta}{\partial y}\right)+(\gamma-1)M_e^2\mu\left(\frac{\partial u}{\partial y}\right)^2, \tag{5a}$$

$$\rho u\frac{\partial u}{\partial x}+\rho\tilde{v}\frac{\partial u}{\partial y}=\frac{1}{r}\frac{\partial}{\partial y}\left(r\mu\frac{\partial u}{\partial y}\right), \tag{5b}$$

$$\frac{\partial}{\partial x}(r\rho u)+\frac{\partial}{\partial y}(r\rho\tilde{v})=0, \tag{5c}$$

$$\gamma M_e^2 p=\rho\theta, \tag{5d}$$

$$r=1+y. \tag{5e}$$

In (5), M_e is the edge Mach number and Pr is the Prandtl number defined as follows:

$$Pr=\bar{\mu}_e\bar{C}_p/\bar{\kappa}_e \tag{6}$$

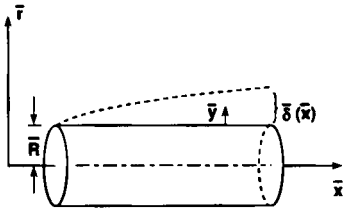

Figure 2. Co-ordinate system and notation for the boundary layer on a circular cylinder

To derive (5), we have made use of the following relationships for thermally perfect gases:[1]

$$\gamma=\bar{C}_p/\bar{C}_v, \qquad \bar{R}_g=\bar{C}_p-\bar{C}_v, \qquad \bar{\rho}_e\bar{u}_e^2=\gamma\bar{p}_eM_e^2, \tag{7}$$

where $\bar{C}_v$ is the specific heat at constant volume, assumed to be constant. Since both $\bar{C}_p$ and $\bar{C}_v$ have been assumed constant, the ratio of specific heats, γ, is constant by definition and the governing equations are strictly valid only for thermally and calorically perfect gases.

In the absence of a pressure gradient, pressure is constant (arbitrary) and the equation of state (5d) is taken to be

$$\rho\theta=1. \tag{8}$$

In dimensionless form the Sutherland viscosity (conductivity) law becomes

$$\mu(\theta)=\kappa(\theta)=\frac{\theta^{3/2}(1+C)}{\theta+C}, \qquad C=\frac{198{\cdot}6\ \text{(Rankine)}}{\bar{T}_e\ \text{(Rankine)}}, \tag{9}$$

There are several reasons why further transformation is desirable prior to attempting numerical solution of the boundary layer equations. Equations (5) in their present form are singular at $x=0$. By appropriate co-ordinate transformation $\zeta=\zeta(x, y)$, $\eta=\eta(x, y)$ the singularity is removed, the governing system is simplified and the growth of the boundary layer in the transform (ζ, η)-plane is reduced, thereby facilitating the numerical method.

Motivated by the 'root x' growth characteristic of laminar boundary layers, we define

$$\zeta(x, y)=\sqrt{(2x)}, \tag{10a}$$

$$\eta(x, y)=y/\sqrt{(2x)}. \tag{10b}$$

The Jacobian corresponding to transformation (10) is

$$\begin{bmatrix}\partial\zeta/\partial x & \partial\zeta/\partial y\\ \partial\eta/\partial x & \partial\eta/\partial y\end{bmatrix}=\begin{bmatrix}1/\zeta & 0\\ -\eta/\zeta^2 & 1/\zeta\end{bmatrix}. \tag{11}$$

After straightforward manipulation of (5) using (10) and (11) we arrive at the governing energy, momentum and continuity equations in the transform (ζ, η)-plane:

$$\zeta f\frac{\partial\theta}{\partial\xi}=g\frac{\partial\theta}{\partial\eta}+\frac{1}{Pr}\frac{\partial}{\partial\eta}\left(\tilde{\kappa}\frac{\partial\theta}{\partial\eta}\right)+(\gamma-1)M_e^2\tilde{\mu}\left(\frac{\partial u}{\partial\eta}\right)^2, \tag{12a}$$

$$\zeta f\frac{\partial u}{\partial\zeta}=g\frac{\partial u}{\partial\eta}+\frac{\partial}{\partial\eta}\left(\tilde{\mu}\frac{\partial u}{\partial\eta}\right), \tag{12b}$$

$$\frac{\partial g}{\partial\eta}=f+\zeta\frac{\partial f}{\partial\zeta}. \tag{12c}$$

Here the following definitions have been exploited for convenience:

$$\tilde{\mu}=r\mu, \qquad \tilde{\kappa}=r\kappa, \qquad f=r\rho u, \qquad g=r\rho(\eta u-v), \qquad v=\tilde{v}/\zeta. \tag{13}$$

In the transform co-ordinates the radial co-ordinate $r(\zeta, \eta)$ assumes the form

$$r=1+\zeta\eta. \tag{14}$$

Transformation (10) is essentially that proposed by Duck[10] for the cylindrical boundary layer, which we prefer here for purposes of clarity. The reader is cautioned, however, that the form of the transformation has considerable impact on the performance of the numerical method, by influencing the condition number of the Jacobian matrices associated with iteration schemes. Our experience has been that the more complicated co-ordinate transformation found in Reference 3 is preferred for adaptation of this method to the boundary layer of a cone.

We make several observations regarding governing system (12). Governing energy (12a) and momentum (12b) equations are parabolic with streamwise variable ζ as timelike. However, as pointed out by Blottner,[2] the boundary layer equations are not the usual (Cauchy) type of initial value problem, because the timelike derivative of g does not appear. It is therefore more appropriate to think of system (12) as defining a constrained evolution problem in which continuity equation (12c) poses a constraint on θ and u. Another peculiarity, which accounts partially for the difficulty encountered in attempts to use fully explicit methods to march the solution away from $\zeta=0$, is the factor ζ preceding timelike derivatives. Whenever $\zeta=0$, $r=1$, timelike derivatives vanish and the solution to (12) is the similarity solution for flow over a flat plate. For $\zeta>0$, self-similarity ($\partial/\partial\zeta=0$) is destroyed by the dependence of the right-hand side on ζ through the radial co-ordinate r.

Boundary and initial conditions

The mathematical formulation of the governing parabolic system of equations (12) is completed by specification of boundary and initial conditions. At the wall, no-slip conditions on velocity lead to

$$u(\zeta, 0)=g(\zeta, 0)=f(\zeta, 0)=0. \tag{15}$$

For the energy equation we consider either fixed temperature or adiabatic wall conditions, (16a) or (16b) respectively, where subscript 'w' denotes the wall value:

$$\theta(\zeta, 0)=\theta_w=\bar{T}_w/\bar{T}_e, \tag{16a}$$

$$\partial\theta(\zeta, 0)/\partial\eta=0. \tag{16b}$$

At the outer edge of the boundary layer $\eta=\eta_{MAX}$, where η_{MAX} is a large but finite distance (chosen on the basis of experience), we assume that temperature and velocity have attained their respective edge values, in which case

$$\theta(\zeta, \eta_{MAX})=u(\zeta, \eta_{MAX})=1. \tag{17}$$

The necessity of a corresponding far-field boundary condition on g is eliminated by the integral treatment of the continuity equation addressed in the next section. Therefore $g(\zeta, \eta_{MAX})$ remains unspecified.

Regarding the initial condition, we adopt the conventional practice of using the 'flat plate' ($\zeta=0$) similarity solution to initialize the marching procedure, based on the reasoning that very near the leading edge $\bar{\delta}\ll\bar{R}$ (where $\bar{\delta}$ is the boundary layer displacement thickness) and transverse curvature is insignificant. Ironically then, system (12) defines its own initial condition.

NUMERICAL METHOD

Governing equations (12) define an initial boundary value problem (IBVP). In the timelike ζ-direction we make straightforward use of fully implicit, high-order, backward finite differencing to march the solution forward. For this purpose it is most convenient to use equal step widths $\Delta\zeta$ whereby

$$\zeta_i = i\Delta\zeta, \quad i=0, 1, 2, \ldots . \tag{18}$$

In the wall-normal η-direction we exploit a spectral collocation method, where 'spectral' refers to the approximation of the continuous operator $\partial/\partial\eta$ by a spectrally accurate discrete operator $\mathbf{L}_N$ and where 'collocation' refers to the error norm; i.e. the residuals of the discretized governing equations are required to vanish identically at each of $N+1$ collocation points $\{\eta_j: j=0, 1, 2, \ldots, N\}$.

Transverse mapping and computational domain

It is both necessary and desirable to incorporate co-ordinate stretching in the wall-normal direction. It is necessary to order to map the physical domain $0 \leqslant \eta \leqslant \eta_{MAX}$ onto the natural domain of the (Chebyshev) spectral collocation method, $-1 \leqslant \tilde{\eta} \leqslant 1$. Furthermore, by judicious choice of the mapping function, collocation points η_j are redistributed and concentrated in the region of high gradients (i.e. at the wall), thereby reducing significantly the number of grid points needed for adequate resolution. For the boundary layer problem the following transformation has proven useful:[5]

$$\eta = \frac{0{\cdot}5\eta_{MAX}(1-\tanh\sigma)(1-\tilde{\eta})}{1-\tanh[0{\cdot}5\sigma(1-\tilde{\eta})]} . \tag{19}$$

In (19), σ is a free parameter which controls the strength of stretching.

The locations of the collocation points will be made precise shortly; however, they are in general unequally spaced and therefore we define

$$\Delta\eta_{j-1} = \eta_j - \eta_{j-1}, \quad j=1, 2, \ldots, N. \tag{20}$$

Discretization of the computational (ζ, η)-domain is shown schematically in Figure 3. For brevity in the discussion to follow, we adopt the following conventions and similar conventions for θ, g and f:

$$u_{ij} = u(\zeta_i, \eta_j), \qquad \mathbf{u}_i = \begin{bmatrix} u_{i,0} \\ u_{i,1} \\ \vdots \\ u_{i,N} \end{bmatrix} . \tag{21}$$

Timelike discretization

Let ϕ be a continuous function of ζ and denote $\phi_i = \phi(\zeta_i)$.Then the fully implicit, backward difference approximation of order M to derivative $\phi'(\zeta_i)$, for equal increments $\Delta\zeta$, is given by

$$\frac{d\phi}{d\zeta}(\zeta_i) = \sum_{m=0}^{M} t_m \phi_{i-m} + O[(\Delta\zeta)^M], \tag{22}$$

where coefficients t_m for methods up to order five are given in Table I. For $M=1$ and 2 equation (22) defines the familiar backward Euler and three-point backward difference methods respectively.

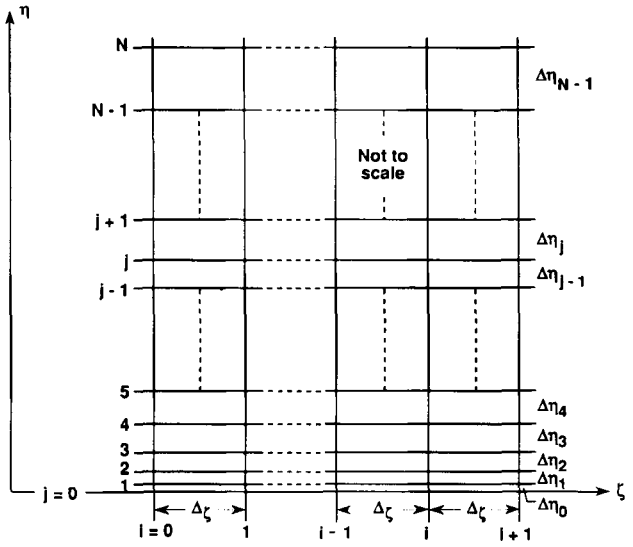

Figure 3. Computational domain

Table I. Coefficients for backward difference methods up to order five

		Backward difference coefficients					
Order M	Factor d	t_0/d	t_1/d	t_2/d	t_3/d	t_4/d	t_5/d
1	$1/\Delta\zeta$	1	−1				
2	$1/2\Delta\zeta$	3	−4	1			
3	$1/6\Delta\zeta$	11	−18	9	−2		
4	$1/24\Delta\zeta$	50	−96	72	−32	6	
5	$1/120\Delta\zeta$	274	−600	600	−400	150	−24

From (22) and vector notation (21) we derive discrete approximations, each with $O[(\Delta\zeta)^M]$ truncation error, for the left-hand sides of the energy (**eLHS**$_i$) and momentum (**mLHS**$_i$) equations and the right-hand side of the continuity (**cRHS**$_i$) equation, whose components are given by

$$\text{eLHS}_{ij}=\zeta_i f_{ij} \sum_{m=0}^{M} t_m \theta_{i-m,j}, \tag{23a}$$

$$\text{mLHS}_{ij}=\zeta_i f_{ij} \sum_{m=0}^{M} t_m u_{i-m,j}, \tag{23b}$$

$$\text{cRHS}_{ij}=f_{ij}+\zeta_i \sum_{m=0}^{M} t_m f_{i-m,j}, \tag{23c}$$

Only for $M=1$ is the fully implicit method self-starting. At the moment we use a scheme of order $M=5$ which takes four initial steps of orders one, two, three and four before settling into fifth-order accuracy. Although formal accuracy is degraded by the initial low-order steps, in practice the error is insignificant for small $\Delta\zeta$, since the boundary layer evolves slowly in the transform (ζ, η)-plane and since the marching is in ζ and not x.

Spectral collocation

A clear and concise introduction to spectral methods can be found in a report 'Spectral methods for CFD' by Zang *et al.*;[12] further detail, theory and examples are available in the recent text by Canuto *et al.*[13] Consequently, we provide minimal theory and detail here and refer the reader to these references for greater depth.

In general, spectral methods are based upon the approximation of a continuous function $\phi(\tilde{\eta})$ on $[-1, 1]$ by a finite series expansion $\phi_N(\tilde{\eta})$ in an orthogonal basis set $B_n(\tilde{\eta})$, namely

$$\phi_N(\tilde{\eta}) = \sum_{n=0}^{N} \hat{\phi}_n B_n(\tilde{\eta}), \tag{24}$$

where coefficients $\hat{\phi}_n$ are termed the 'spectrum' of $\phi_N(\tilde{\eta})$. For non-periodic problems an appropriate basis is the set of Chebyshev polynomials

$$B_n(\tilde{\eta}) = T_n(\tilde{\eta}) = \cos(n\cos^{-1}\tilde{\eta}), \tag{25}$$

for which the Gauss–Lobatto set (26) is a corresponding natural set of collocation points:

$$\tilde{\eta}_j = \cos\gamma_j, \quad \gamma_j = \pi j/N, \qquad j = 0, 1, 2, \ldots, N. \tag{26}$$

Set (26) is 'natural' in the sense that (25) and (26) render (24) a discrete Fourier cosine transform:

$$\phi_j = \phi_N(\tilde{\eta}_j) = \sum_{n=0}^{N} \hat{\phi}_n \cos\frac{n\pi j}{N}. \tag{27}$$

To evaluate the spectra $\hat{\phi}_n$, the corresponding discrete inverse transform[12] is

$$\hat{\phi}_n = \frac{2}{Nc_n} \sum_{j=0}^{N} \frac{\phi_j}{c_j} \cos\frac{n\pi j}{N}, \tag{28}$$

where

$$c_j = \begin{cases} 2, & j = 0 \text{ or } N, \\ 1, & 0 < j < N. \end{cases} \tag{29}$$

Interpreted in the light of transformation pair (27) and (28), (24) defines the spectral interpolation polynomial, exact by definition at the collocation points. Unlike polynomial interpolating series defined on equally spaced intervals, series (24) converges uniformly to $\phi(\tilde{\eta})$ as $N \to \infty$. Moreover, it can be shown[12] that for continuously differentiable functions ϕ, coefficients $\hat{\phi}_n$ decay to zero faster than any finite power of $1/N$ as $N \to \infty$. This is termed 'spectral convergence'.

Other orthogonal bases (e.g. Legendre polynomials) are possible and lead to corresponding transforms and collocation sets. An advantage of the Chebyshev polynomial basis, however, is that (27) and (28) yield to efficient fast transform techniques.

It follows from (24) and (25) that derivative $\phi'_N(\tilde{\eta})$ is given at collocation point $\tilde{\eta}_j$ by

$$\frac{\mathrm{d}\phi_N}{\mathrm{d}\tilde{\eta}}(\tilde{\eta}_j) = \sum_{n=0}^{N} \hat{\phi}_n T'_n(\tilde{\eta}_j). \tag{30}$$

From (30) we derive the following matrix–vector equation for the vector $\boldsymbol{\phi}'$ whose elements are the derivative values at the collocation points:

$$\boldsymbol{\phi}' = \mathbf{D}_N \hat{\boldsymbol{\phi}}, \qquad (\mathbf{D}_N)_{jn} = T'_n(\tilde{\eta}_j). \tag{31}$$

The elements of the matrix $\mathbf{D}_N$ are most easily computed by a recursion relation which can be found in Reference 12. Furthermore, (28) has the matrix–vector form

$$\hat{\boldsymbol{\phi}} = \mathbf{P}_N \boldsymbol{\phi}, \tag{32}$$

where the elements of $\mathbf{P}_N$ are obvious from (28). From (31) and (32) the definition of the spectral differentiation operator $\mathbf{L}_N$ follows immediately,

$$\mathbf{L}_N = \mathbf{D}_N \mathbf{P}_N, \tag{33}$$

whereby

$$\boldsymbol{\phi}' = \mathbf{L}_N \boldsymbol{\phi}. \tag{34}$$

A few comments regarding operator $\mathbf{L}_N$ are in order. When co-ordinate stretching as in (19) is used, the stretching metric is incorporated directly into $\mathbf{L}_N$ through the chain rule and results in the scaling of each row of $\mathbf{L}_N$ by the factor $\partial\tilde{\eta}/\partial\eta$. It should be noted that unlike finite difference differentiation operators, which are banded, spectral operator $\mathbf{L}_N$ is dense. It is precisely this global nature, however, which accounts for the extraordinary accuracy of spectral methods. A bonus of the method is that no special differentiation formulae are needed at boundaries as required by finite difference techniques.

For systems of large N the derivatives (34) are most efficiently computed using fast cosine transforms. However, for moderately sized systems such as is the case here, matrix multiplication is both a simple and efficient method of differentiation which is readily implemented in vector mode on array processors. Consequently, we adopt differentiation by matrix multiplication and forego discussion of transform methods.

Discretization of the right-hand side (RHS) of the energy and momentum equations is completed by approximation of the continuous operator $\partial/\partial\eta$ with its discrete spectral analogue $\mathbf{L}_N$, from which the following vector equations result:

$$\mathbf{eRHS}_i = \mathbf{G}_i \mathbf{L}_N \boldsymbol{\theta}_i + \frac{1}{Pr} \mathbf{L}_N \mathbf{V}_i \mathbf{L}_N \boldsymbol{\theta}_i + (\gamma - 1) M_e^2 \mathbf{V}_i \mathbf{z}_i, \tag{35a}$$

$$\mathbf{mRHS}_i = \mathbf{G}_i \mathbf{L}_N \mathbf{u}_i + \mathbf{L}_N \mathbf{V}_i \mathbf{L}_N \mathbf{u}_i. \tag{35b}$$

Here $\mathbf{G}_i$ and $\mathbf{V}_i$ are diagonal matrices which contain the values g_{ij} and $\tilde{\mu}_{ij} = \tilde{\kappa}_{ij}$ respectively and, if

$$\mathbf{u}_i' = \mathbf{L}_N \mathbf{u}_i, \tag{36}$$

then

$$z_{ij} = (u_{ij}')^2. \tag{37}$$

From (23) and (35) we obtain the residual formulations of the energy and momentum equations:

$$\mathbf{er}_i = \mathbf{eRHS}_i - \mathbf{eLHS}_i, \tag{38a}$$

$$\mathbf{mr}_i = \mathbf{mRHS}_i - \mathbf{mLHS}_i. \tag{38b}$$

There are several reasons why it is advantageous to convert continuity equation (12c) from differential to integral form before formulating its residual equation. First, an integral form reduces by one the number of equations and eliminates the need for the outer boundary condition on g in much the same way that boundary conditions on pressure are eliminated by the use of staggered grids in numerical solutions of the Navier–Stokes equations. Secondly, with regard to the preconditioner to be developed later, integral rather than differential form is preferable for first-order equations. Thirdly, relative to numerical differentiation, numerical integration is a

smoothing operation and tends to diminish round-off error. Therefore, integrating both sides of (12c) between η_{j-1} and η_j, we obtain

$$g(\zeta, \eta_j) - g(\zeta, \eta_{j-1}) = \int_{\eta_{j-1}}^{\eta_j} \left(f + \zeta \frac{\partial f}{\partial \zeta} \right) \mathrm{d}\eta. \tag{39}$$

In a manner analogous to the construction of the spectral differentiation operator $\mathbf{L}_N$, we construct the spectrally accurate, discrete integration operator $\mathbf{N}_N$ to approximate the continuous integral in (39). The following residual form of the continuity equation results:

$$\mathrm{cr}_{ij} = g_{ij} - g_{i,j-1} - h_{ij}, \quad j = 1, 2, \ldots, N, \tag{40}$$

where

$$\mathbf{h}_i = \mathbf{N}_N \mathbf{cRHS}_i. \tag{41}$$

We close this subsection by discussing the construction of the spectral integration operator $\mathbf{N}_N$. Consider the approximation

$$E_j = \int_{\tilde{\eta}_{j-1}}^{\tilde{\eta}_j} \phi_N(\tilde{\eta})\, \mathrm{d}\tilde{\eta} \cong \int_{\tilde{\eta}_{j-1}}^{\tilde{\eta}_j} \phi(\tilde{\eta})\, \mathrm{d}\tilde{\eta}, \quad j = 1, 2, \ldots, N. \tag{42}$$

However,

$$E_j = \int_{\tilde{\eta}_{j-1}}^{\tilde{\eta}_j} \sum_{n=0}^{N} \hat{\phi}_n T_n(\tilde{\eta})\, \mathrm{d}\tilde{\eta} = \sum_{n=0}^{N} \hat{\phi}_n \int_{\tilde{\eta}_{j-1}}^{\tilde{\eta}_j} T_n(\tilde{\eta})\, \mathrm{d}\tilde{\eta}. \tag{43}$$

In matrix–vector form, expression (43) becomes

$$\mathbf{E} = \mathbf{Q}_N \hat{\boldsymbol{\phi}}, \tag{44}$$

where $\mathbf{E}$ is an N-vector and $\mathbf{Q}_N$ is an $N \times (N+1)$ spectral quadrature matrix whose elements are obtained from (43) with the help of (26):

$$q_{jn} = -\int_{\gamma_{j-1}}^{\gamma_j} \sin\gamma \cos(n\gamma)\, \mathrm{d}\gamma, \quad j = 1, 2, \ldots, N, \quad n = 0, 1, 2, \ldots, N. \tag{45}$$

From (44) and (32) the $N \times (N+1)$ spectral integration operator $\mathbf{N}_N$ is defined as

$$\mathbf{N}_N = \mathbf{Q}_N \mathbf{P}_N. \tag{46}$$

As in the case of the spectral differentiation operator, the stretching metric is incorporated directly into $\mathbf{N}_N$.

Preconditioned iteration

The implicit treatment of the timelike derivative and the non-linearity of the governing equations mandate iteration at each marching step. An iterative scheme which fully couples residual equations (38a), (38b) and (40) is preferred in order to enhance convergence. To this end, let solution vector $\mathbf{s}_i^k$, update vector $\Delta\mathbf{s}_i^k$ and residual vector $\mathbf{res}_i^k = \mathbf{res}(\mathbf{s}_i^k)$ be defined as follows, where k denotes the iteration index:

$$\mathbf{s}_i^k = \begin{bmatrix} \mathbf{s}_{i,1}^k \\ \mathbf{s}_{i,2}^k \\ \vdots \\ \mathbf{s}_{i,N-1}^k \end{bmatrix}, \qquad \mathbf{s}_{ij}^k = \begin{bmatrix} \theta_{ij}^k \\ u_{ij}^k \\ g_{ij}^k \end{bmatrix}, \tag{47a}$$

$$\Delta \mathbf{s}_i^k = \begin{bmatrix} \Delta \mathbf{s}_{i,1}^k \\ \Delta \mathbf{s}_{i,2}^k \\ \vdots \\ \Delta \mathbf{s}_{i,N-1}^k \end{bmatrix}, \qquad \Delta \mathbf{s}_{ij}^k = \begin{bmatrix} \Delta\theta_{ij}^k \\ \Delta u_{ij}^k \\ \Delta g_{ij}^k \end{bmatrix}, \tag{47b}$$

$$\mathbf{res}_i^k = \begin{bmatrix} \mathbf{res}_{i,1}^k \\ \mathbf{res}_{i,2}^k \\ \vdots \\ \mathbf{res}_{i,N-1}^k \end{bmatrix}, \qquad \mathbf{res}_{ij}^k = \begin{bmatrix} \mathrm{er}_{ij}^k \\ \mathrm{mr}_{ij}^k \\ \mathrm{cr}_{ij}^k \end{bmatrix}. \tag{47c}$$

For the moment, consider only Dirichlet boundary conditions at both the wall and outer boundary so that residuals $j=0$ and $j=N$ vanish automatically. In the terminology above, the solution $\mathbf{s}_i$ at step i is defined by $\mathbf{res}(\mathbf{s}_i)=\mathbf{0}$. In practice, we accept iterate $\mathbf{s}_i^k$ whenever $|\mathbf{res}(\mathbf{s}_i^k)|_{MAX}<\varepsilon$, where ε is a specified convergence criterion.

A straightforward application of Newton's method for systems is ill-advised for several reasons. First, the dense spectral differentiation and integration operators lead to a relatively large, dense Jacobian $\mathbf{J}$ and a large per-iteration computational workload. Secondly, $\mathbf{J}$ is ill-conditioned and the convergence of Newton's method is suboptimal.

A variant of Newton's method suited to this problem is preconditioned Richardson iteration[6] defined by

$$\mathbf{H}_k \Delta \mathbf{s}_i^k = -\mathbf{res}_i^k, \tag{48a}$$

$$\mathbf{s}_i^{k+1} \leftarrow \mathbf{s}_i^k + \tau \Delta \mathbf{s}_i^k. \tag{48b}$$

Preconditioner $\mathbf{H}$ is a convenient and easily inverted approximation to Jacobian $\mathbf{J}$ and τ is a relaxation parameter used to control the spectral radius of the iteration matrix $\mathbf{M}_k=\mathbf{I}-\tau\mathbf{H}_k^{-1}\mathbf{J}_k$. Provided the initial guess $\mathbf{s}_i^0$ is sufficiently close, spectral radius $(\mathbf{M}_k)<1$ for all k suffices to guarantee convergence.

Any number of suitable preconditioners are possible. For this problem an effective preconditioner $\mathbf{H}$ was derived from finite difference analogues of residual equations (38) and (40). With unknowns ordered according to (47), $\mathbf{H}$ has block tridiagonal structure and step (48a) of the iteration is accomplished efficiently using a block tridiagonal Gaussian elimination algorithm.

Diagonal dominance of the preconditioner is a desirable trait which eliminates the necessity for pivoting or scaling during Gaussian elimination. Consequently, we exploit both one-sided and 'centred' finite difference approximations on non-standard grids to maintain the diagonal dominance of $\mathbf{H}_k$. For example, if **ER**, **MR** and **CR** denote finite difference versions of residual vectors **er**, **mr** and **cr** respectively, then we construct **MR** as follows:

$$\mathrm{MR}_j = g_j\left(\frac{u_j-u_{j-1}}{\Delta\eta_{j-1}}\right) + \frac{1}{\Delta\eta_{j-1}+\Delta\eta_j}\left[(\tilde{\mu}_{j+1}+\tilde{\mu}_j)\left(\frac{u_{j+1}-u_j}{\Delta\eta_j}\right)-(\tilde{\mu}_j+\tilde{\mu}_{j-1})\left(\frac{u_j-u_{j-1}}{\Delta\eta_{j-1}}\right)\right]$$
$$-\mathrm{mLHS}_i, \qquad j=1, 2, \ldots, N-1. \tag{49}$$

In (49) and in the discussion to follow, the subscript i has been dropped for clarity. Note that the first derivative term in (49) is approximated by a first-order backward difference quotient. In contrast, the approximation of operator $(\partial/\partial\eta)\tilde{\mu}\partial/\partial\eta$ is of $O(\Delta\eta_j\Delta\eta_{j-1})$ accuracy and is derived from the difference quotient of two second-order centred difference approximations at fictitious

points $\eta_{j-1/2}$ and $\eta_{j+1/2}$. Components of **ER** are defined analogously and are omitted here. For preconditioning the continuity equation, the trapezoid qudrature rule provides a convenient finite difference integration operator analogous to $\mathbf{N}_N$ and leads to the following analogue of (40):

$$\mathrm{CR}_j = g_j - g_{j-1} - \frac{\Delta\eta_{j-1}}{2}(h_j + h_{j-1}), \quad j = 1, 2, \ldots, N. \tag{50}$$

Preconditioner **H** is now defined as the Jacobian of the finite difference residual equations, ordered according to (47). Correspondingly, **H** is of block tridiagonal structure as follows:

$$\mathbf{H} = \begin{bmatrix} \mathbf{B}_1 & \mathbf{C}_1 & & & \\ \mathbf{A}_2 & \mathbf{B}_2 & \mathbf{C}_2 & & \\ & \ddots & \ddots & \ddots & \\ & & \mathbf{A}_{N-1} & \mathbf{B}_{N-1} & \end{bmatrix}, \tag{51}$$

where $\mathbf{A}_j$, $\mathbf{B}_j$ and $\mathbf{C}_j$ are each 3×3 matrices. Specifically, matrices $\mathbf{B}_j$ are defined by

$$\mathbf{B}_j = \begin{bmatrix} \partial \mathrm{ER}_j/\partial\theta_j & \partial \mathrm{ER}_j/\partial u_j & \partial \mathrm{ER}_j/\partial g_j \\ \partial \mathrm{MR}_j/\partial\theta_j & \partial \mathrm{MR}_j/\partial u_j & \partial \mathrm{MR}_j/\partial g_j \\ \partial \mathrm{CR}_j/\partial\theta_j & \partial \mathrm{CR}_j/\partial u_j & \partial \mathrm{CR}_j/\partial g_j \end{bmatrix}, \quad j = 1, 2, \ldots, N-1. \tag{52}$$

Matrices $\mathbf{A}_j$ and $\mathbf{C}_j$ are defined similarly except that the lower indices are $j-1$ and $j+1$ respectively.

We complete discussion of the preconditional iteration by addressing some remaining loose ends.

Since g_N is unspecified, there is a 'stray' residual equation for cr_N to satisfy. The update equation which defines Δg_N is given below and is derived from the residual equations for cr_N and CR_N:

$$\Delta g_N = \Delta g_{N-1} + 0{\cdot}5(1 + \zeta t_0)\Delta\eta_{N-1}\left(\frac{r_{N-1}}{\theta_{N-1}}\Delta u_{N-1} - \frac{f_{N-1}}{\theta_{N-1}}\Delta\theta_{N-1}\right) + \mathrm{cr}_N. \tag{53}$$

Because of the integral treatment of (12c), (53) decouples from system (48a) and is solved subsequently.

In the case of adiabatic wall boundary condition (16b) for temperature, system (48a) is appended by an additional equation

$$c_0\Delta\theta_0 + c_1\Delta\theta_1 + c_2\Delta\theta_2 = 0, \tag{54}$$

where coefficients c_0, c_1 and c_2 are obtained from the three-point forward difference approximation of $\partial\theta/\partial\eta$ on a non-standard mesh. Vector $\Delta\mathbf{s}_1$ is extended to incorporate $\Delta\theta_0$ and results in blocks $\mathbf{B}_1$ and $\mathbf{C}_1$ of dimensions 4×4 and 4×3 respectively. Modification of the block tridiagonal algorithm is straightforward if the directions of 'forward' elimination and 'back' substitution are reversed. Following the update step (48b), θ_0 is defined by the requirement

$$\mathbf{L}_N\boldsymbol{\theta}|_0 = 0. \tag{55}$$

We note that the preconditioner currently in use does not model the variation of viscosity with temperature except in the dissipation term of the energy equation, since the additional terms tend to destroy diagonal dominance.

Finally, we note that iteration (48) can be rendered parameter-free and convergence ehnanced dramatically by a residual minimization technique similar to that proposed by Malik *et al.*[14] at a

cost of approximately double the per-iteration computational workload. We have chosen not to incorporate this optimization for the one-dimensional spectral method at hand. However, for spectral approximations in two or more dimensions, such refinement is recommended by considerations of computational efficiency.

Algorithm

For completeness, we summarize an algorithm which embodies the numerical method detailed in this section:

initialization
  define ε, $\Delta\zeta$, N, etc.
  $k \leftarrow 0$
  initial guess $\mathbf{s}_0^0$
for marching steps $i = 0, 1, 2, \ldots$

$\zeta_i \leftarrow i\Delta\zeta$
repeat while $|\mathbf{res}_i^k|_{MAX} > \varepsilon$

  compute residuals $\mathbf{res}_i^k$ spectrally
  compute preconditioner $\mathbf{H}^k$ by finite differences
  solve $\mathbf{H}^k \Delta\mathbf{s}_i^k = -\mathbf{res}_i^k$
  perform update $\mathbf{s}_i^{k+1} \leftarrow \mathbf{s}_i^k + \tau\Delta\mathbf{s}_i^k$
  $k \leftarrow k+1$

initialize for next step $\mathbf{s}_{i+1}^0 \leftarrow \mathbf{s}_i^k$
$k \leftarrow 0$

Note that computation of the initial condition $\mathbf{s}_0$ is performed within the algorithm for $i = 0$ and requires no special treatment except the following. Since timelike derivative terms contribute to the diagonal dominance of the preconditioner, it is necessary to restrict τ for the $i = 0$ step and to expect slower convergence.

Before proceeding to the Results section, we offer a couple of recommendations regarding accurate and efficient implementation of the algorithm described above. In any spectral method applied to a non-linear problem, numerical instability due to aliasing error arises if resolution is inadequate. Our preference, rather than resorting to de-aliasing devices, is to maintain sufficient resolution N so that aliasing errors are negligibly small. A practical guide to the adequacy of resolution is the decay rate of the 'tail' of the spectrum of Chebyshev coefficients, as will be illustrated in the Results section. Finally, it is recommended that computations for the spectral differentiation and integration matrices $\mathbf{L}_N$ and $\mathbf{N}_N$ be performed in double-precision arithmetic in order to limit round-off error. Since the operators need be computed only once, the additional computational effort is insignificant.

NUMERICAL RESULTS

As suggested in the Introduction, this work has been motivated by its applicability in the area of stability and transition for compressible flows. In the past few years at NASA Langley Research Center, effort has been expended to develop efficient and spectrally accurate computer codes to

solve the eigenvalue problems associated with temporal linear stability analyses of high-speed, compressible flows. Additional effort has been devoted to developing spectral codes for fully non-linear simulation of stability and transition. Although, with sufficiently fine grid resolution, finite difference codes can provide the highly accurate mean flow profiles needed for linear stability analyses and non-linear simulations, the interpolation from finite difference to spectral grids is problematic and a source of error, particularly when co-ordinate stretching is involved. In short, this work was initiated in order to provide boundary layer profiles of spectral accuracy for spectrally accurate stability codes. Accordingly, our purpose in this section is threefold: to offer reasonable validation of the spectral method; to present results of application of the method to a particular test problem; and to discuss briefly implications of these results for viscous, linear stability theory.

Test case

The model problem which we examine is that of computing boundary layer velocity and temperature profiles along a cylindrical 'fuselage' of radius $\bar{R}=10$ ft for a high-speed flow at Mach 5 and altitude 150 000 ft. The particular parameter values and dimensional quantities associated with the test problem are the following, which have been derived with the help of standard atmospheric tables and isentropic gas relationships:[11]

$$M_\infty=5, \quad \gamma=1{\cdot}4, \quad Pr=0{\cdot}72, \quad \bar{R}=10\text{ ft}, \quad \bar{T}_\infty=480\,^\circ\text{R},$$
$$\bar{T}_{t_\infty}=2880\,^\circ R, \quad \bar{P}_{t_\infty}=1500\text{ lb/ft}^2, \quad Re_1=52\,534{\cdot}28\text{ ft}^{-1}, \quad Re=525\,342{\cdot}8. \tag{56}$$

In (56), subscript ∞ refers to pre-shock freestream conditions, subscript 't' denotes total (stagnation) conditions, Re_1 is the unit freestream Reynolds number and dimensional quantities are expressed in British units. For the scenario of flow along a cylinder, the bow shock wave is weak and very oblique, so that for all practical purposes the freestream and edge conditions are identical. However, we caution that in general this is not the case and post-shock conditions must normally be computed from, say, Reference 11. We summarize the parameter values for the test case below, noting that radius $\bar{R}$ and Reynolds number scale out of the dimensionless governing equations:

$$M_e=5, \quad Pr=0{\cdot}72, \quad \gamma=1{\cdot}4, \quad \bar{T}_e=480\,^\circ\text{R}. \tag{57}$$

To complete specification of the test case, let us also assume that the fuselage wall is insulated so that the appropriate boundary condition is (16b)

Validation

The next few figures and tables compare results obtained by the spectral collocation method with those computed by a second-order, finite difference standard, the boundary layer code of Harris and Blanchard.[3] It is important that only converged solutions be compared and therefore we monitor two indicators of convergence: the point value of wall temperature θ_w and the integral quantity δ_η defined by

$$\delta_\eta=\int_0^{\eta MAX}(1-\rho u)\,d\eta. \tag{58}$$

Table II shows the variation of these two indicators with refinement of the finite difference mesh at the initial station ($x=0$) and suggests that both quantities have converged to five-place accuracy for $N=400$. As the mesh is further refined (not shown), round-off error dominates and

Table II. Convergence of the finite difference method with increasing resolution

	Convergence indicators	
N	δ_η	θ_w
25	6·662922	4·911289
50	6·991767	5·184364
100	7·007874	5·191081
200	7·008662	5·191328
400	7·008684	5·191344

Table III. Convergence of the spectral method with increasing resolution

	Convergence indicators	
N	δ_η	θ_w
26	7·022979757	5·208872370
41	7·013028890	5·194176396
65	7·010044140	5·191963437
77	7·009978464	5·191900431
82	7·009964113	5·191884777
92	7·009965493	5·191887017
101	7·009964420	5·191885558
111	7·009963745	5·191884789
121	7·009963850	5·191884912
127	7·009963854	5·191884917

the values of δ_η and θ_w diverge. Therefore we accept the solution for $N=400$ as the converged finite difference 'initial' condition. Corresponding information for the spectral method is presented in Table III. Here δ_η is computed by a spectrally accurate quadrature law (whereas the trapezoid quadrature rule is used for the finite difference method). For the spectral method, two-place accuracy is obtained with 27 collocation points; five-place accuracy results from 77 points and the solution has converged to nine places with 127 points. Further indication of the adequacy of the resolution of the spectral method is shown in Figure 4, in which the magnitudes of the components of the spectrum, $\bar{u}_j$, are seen to have decayed by 10 orders of magnitude for $i=0$ and $N=110$. The linear decay rate of the spectrum on a logarithmic scale is indicative of spectral convergence. The converged finite difference solution and the spectral solution for $N>40$ agree to three significant figures and, as shown in Figure 5, the respective streamwise velocity profiles are indistinguishable in graphical format. For both computations, $\eta_{MAX}=21$, so that the far-field boundary condition is applied at a distance of approximately three displacement thicknesses from the wall. It should be noted that the stretching metrics differ for the two methods. The finite difference scheme incorporates exponential stretching away from the wall whereas the spectral scheme relies on (19) with $\sigma=1{\cdot}2$.

Figures 6 and 7 compare the evolution of the boundary layer along a cylinder as computed by the two different schemes. For both methods the solution is marched downstream a distance of 10

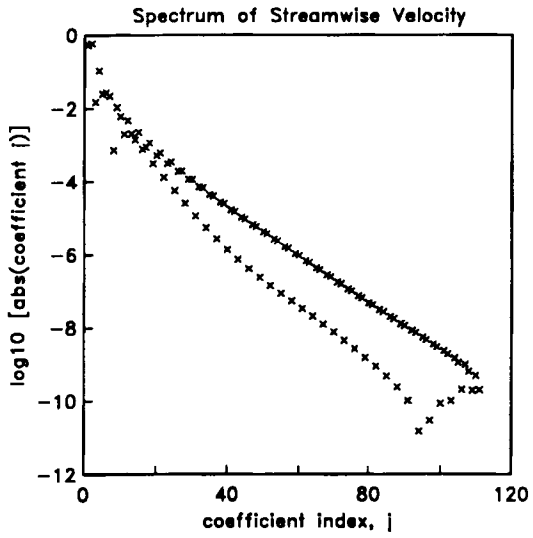

Figure 4. Spectrum of the streamwise velocity for $N = 110$

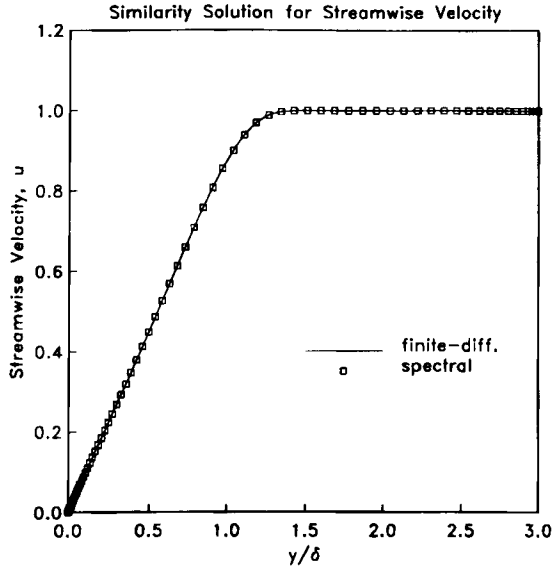

Figure 5. Similarity solution for streamwise velocity

body radii, starting from the respective converged 'initial' similarity profiles at $x = \zeta = 0$. For the finite difference standard, which has second-order accuracy in x, 200 equal marching steps are taken, each of 0·5 ft. Because of the higher-order (fifth) streamwise accuracy of the spectral scheme and because the marching is in ζ not x, only six coarse steps of equal width $\zeta = 1{\cdot}028 \times 10^{-3}$ are taken. Figure 6 compares the growth of the boundary layer displacement thickness $\bar{\delta}$ versus

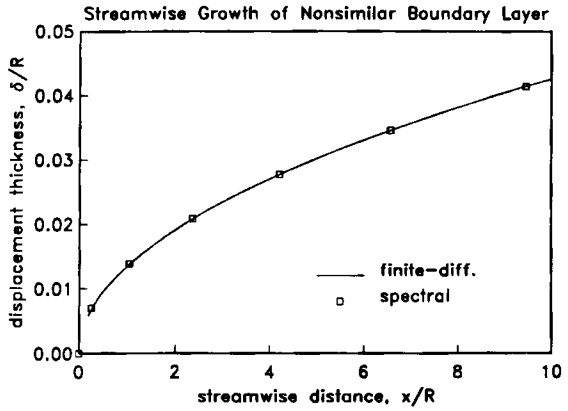

Figure 6. Streamwise growth of boundary layer displacement thickness along a cylinder

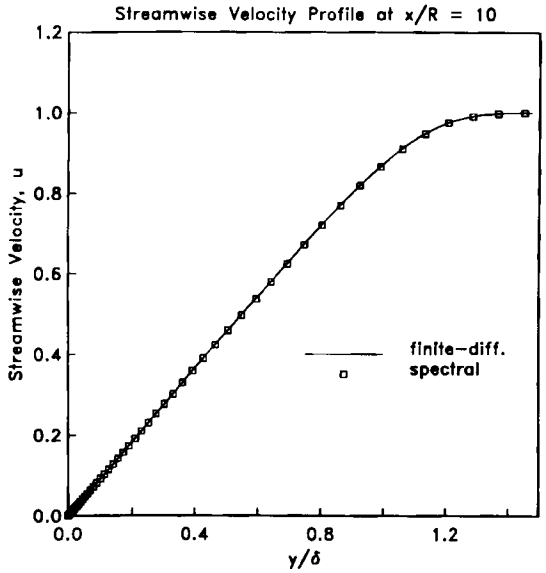

Figure 7. Streamwise velocity profile at station $\bar{x}/\bar{R}=10$

streamwise distance for the two methods, where $\bar{\delta}$ is defined by

$$\bar{\delta}=\int_0^\infty \left(1-\frac{\bar{\rho}\bar{u}}{\bar{\rho}_e\bar{u}_e}\right) d\bar{y}. \tag{59}$$

The agreement in the computed displacement thickness at the final station is to three significant digits. Moreover, Figure 7 shows excellent pointwise agreement in the streamwise velocity profiles at the final station.

Regarding computational efficiency of the spectral algorithm, the computation above for values $N=76$ and $\varepsilon=10^{-8}$ required about 6 CPU seconds on a Cray 2, less than 1 CPU second per marching step for $i>0$. Figure 8 compares the convergence history of the $i=0$ and $i=6$

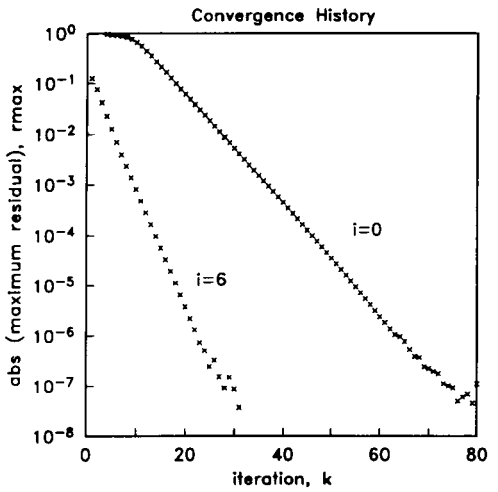

Figure 8. Convergence history of the preconditioned iteration for $N = 76$

iterations, for which respective values of $\tau = 0{\cdot}25$ and $\tau = 0{\cdot}4$ were used. Convergence of the former iteration is slower not only because of the smaller value of the relaxation parameter but also because the initial guess $\mathbf{s}_0^0$ is relatively crude. It should be noted that the $M_e = 5$ case is a fairly stringent test of the method since the preconditioner tends to become ill-conditioned at higher values of Mach number. Without the use of double-precision arithmetic in the computation of the residuals it is not possible to drive the maximum residual of the energy equation below 10^{-8}. In contrast, we attain maximum residual values of the order of 10^{-12} using single precision for $M_e = 1{\cdot}6$.

Implications for linear stability theory

In the past few years, transition researchers have begun to examine the effects of transverse curvature on the stability of flows over axisymmetric bodies. Mack's pioneering work[15] on the stability of compressible flow has encouraged others in that, despite simplifying assumptions, he has obtained fair quantitative agreement between linear stability theory and experiment for hypersonic flow over a sharp cone.[16] Recently, Kao and Chow have exploited spectral methods to study the stability of incompressible flow along cylinders[17] and blunt cylinders.[18] Inviscid, axisymmetric instability modes in the boundary layer of a cylinder have been investigated by Duck,[10] by means of finite difference methods, for Mach numbers of 2·8 and 3·8. In a recent report, Malik and Spall[7] document the effects of curvature on both axisymmetric and asymmetric instability modes in Mach 5 flow over cylinders and sharp cones. The results presented here are intented to parallel those of Malik and Spall. However, we incorporate a temporal rather than spatial model of stability and we exploit spectral rather than finite difference numerical methods.

In the boundary layer of an axisymmetric body, transverse curvature affects stability both directly through curvature terms in the stability equations and indirectly through modification of the underlying mean velocity and temperature profiles. Streamwise evolution of these mean flow profiles is portrayed in Figure 9, obtained by the spectral collocation algorithm. Each profile of the family is uniquely identified by a particular value of curvature K defined unambiguously by

$$K = \bar{\delta}/\bar{R} = \zeta\delta_\eta. \tag{60}$$

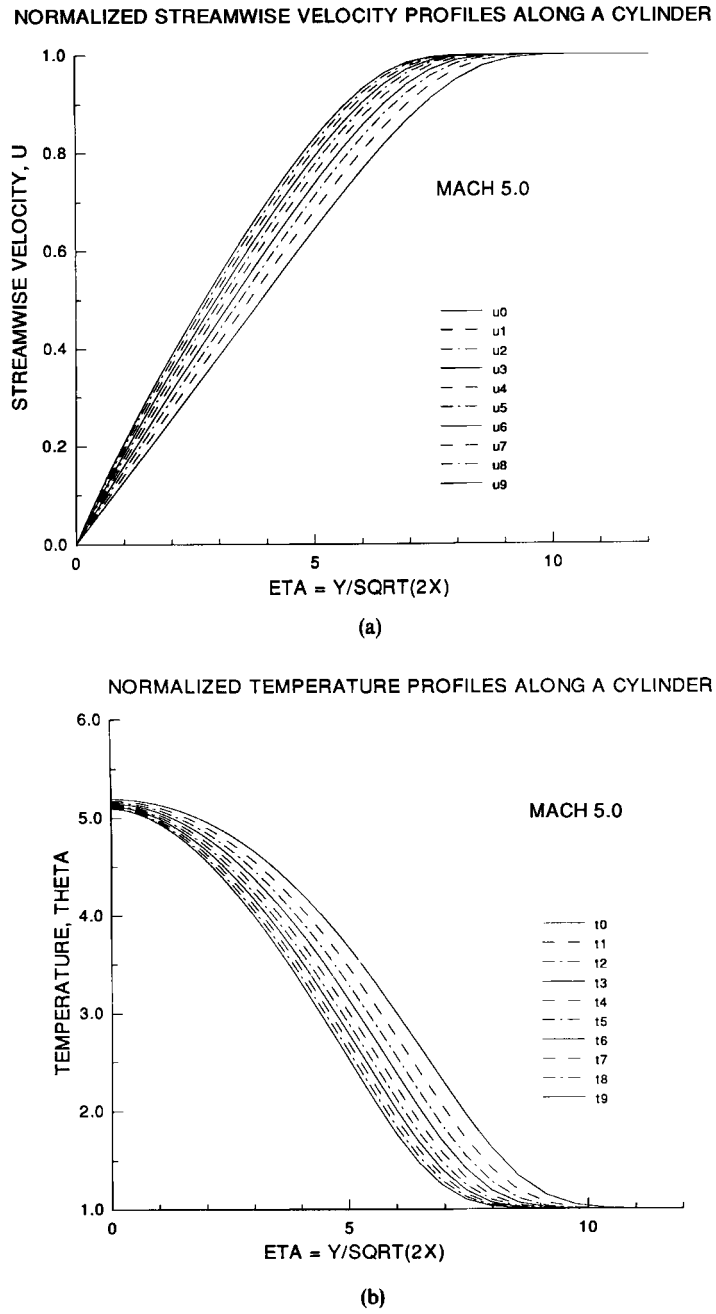

Figure 9. Streamwise evolution of (a) normalized velocity and (b) temperature profiles in the boundary layer of a cylinder in Mach 5 flow: (0) $K=0$; (1) $K=0{\cdot}133$; (2) $K=0{\cdot}256$ (3) $K=0{\cdot}371$; (4) $K=0{\cdot}48$; (5) $K=0{\cdot}585$; (6) $K=0{\cdot}686$; (7) $K=0{\cdot}784$; (8) $K=0{\cdot}879$; (9) $K=0{\cdot}972$

The rightmost profiles ($K=0$) correspond to the initial $\xi=0$ station where displacement thickness is insignificant relative to radius. On the other hand, the leftmost profiles correspond to a station far downstream where boundary layer displacement thickness and radius are of approximately equal magnitudes. For the large unit Reynolds numbers encountered in most flight regimes, $O(1)$-curvature in aerodynamic applications is unlikely. For example, the final station ($\bar{x}/\bar{R}=10$) of Figures 6 and 7 corresponds to a curvature value of only 0·0425. However, as the results presented below will show, even moderate curvature, say $0{\cdot}01<K<0{\cdot}1$, may significantly influence stability.

The 'flat plate' ($K=0$) profiles of Figure 9 also illustrate some of the effects of compressibility when compared to, say, the Blasius solution for incompressible flow over a flat plate.[8] First, the temperature variation across the boundary layer increases with increasing M_e; at $M_e=5$ the wall temperature is more than five times that at the edge of the boundary layer. Secondly, the boundary layer thickens with increasing M_e; at $M_e=5$ the displacement thickness is roughly seven times that for incompressible flow. Thirdly, the u-velocity profile tends to 'flatten' with increasing Mach number.

Figures 10, 12 and 13 display the influence of increasing transverse curvature K on certain instability modes in the boundary layer of a cylinder. Data for these figures are derived from the spectral boundary layer code described herein and SPECLS, a spectrally accurate stability code developed by Macaraeg *et al.*[19] to solve the eigenvalue problems which arise in viscous linear stability theory. Given the Reynolds number based on displacement thickness, $Re_{\bar{\delta}}$, the dimensionless radius $R=\bar{R}/\bar{\delta}=1/K$ and wave numbers $\alpha=\bar{\alpha}\bar{\delta}$ and $\beta=\bar{\beta}\bar{\delta}$, SPECLS returns the eigenvalue $\omega=\omega_r+i\omega_i$ (and associated eigenfunction), where ω_r is the circular frequency of the instability wave and ω_i is its (temporal) growth rate.

A point of reference of the discussion to follow can be found in the neutral stability curves given by Mack[15] in his review of boundary layer stability theory. We summarize briefly some relevant points. For Mach numbers above 2·2, different types of instability modes can coexist. So-called 'first-mode' instabilities exhibit both viscous and inviscid nature, are characterized by relatively low frequencies (wave numbers) and are most unstable when oblique. In contrast, 'second-mode' instabilities are predominantly inviscid in nature, are characterized by high frequencies (wave numbers) and are most unstable when propagating in the direction of flow ($\beta=0$). The second mode is maximally unstable at $M_e=4{\cdot}5$, with a growth rate several times that of the most unstable

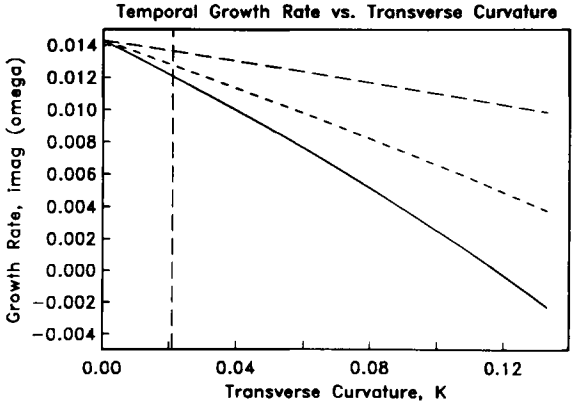

Figure 10. Variation in temporal growth rate of an axisymmetric second-mode instability wave subject to increasing transverse curvature: ——, combined effect; – – –, indirect effect; - - -, direct effect

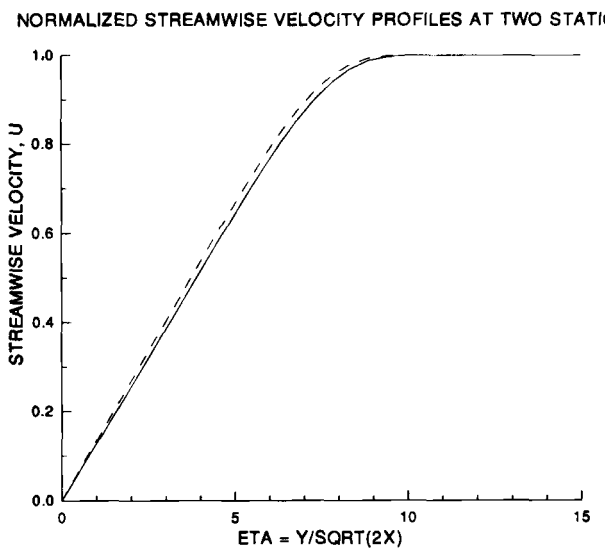

Figure 11. Normalized streamwise velocity profiles at two stations: ——, $K=0$; – – –, $K=0{\cdot}0815$

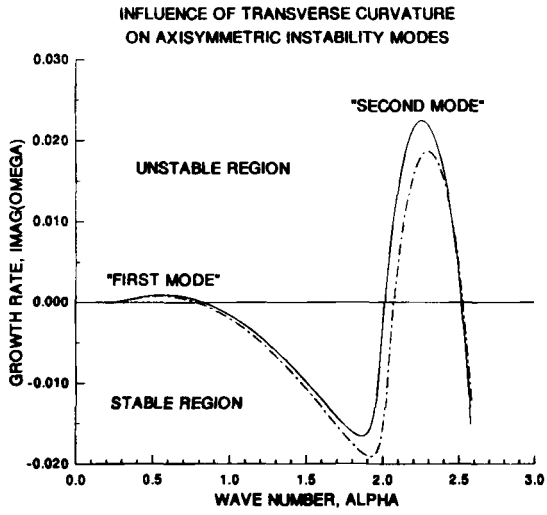

Figure 12. Influence of transverse curvature on axisymmetric instability modes at Mach 5: ——, $K=0$; – · –, $K=0{\cdot}815$

first-mode instability. Of Mack's neutral stability curves, that for $M_e=4{\cdot}8$ flow over a flat plate corresponds most closely with the test cases presented below, although we point out that it was computed for wind tunnel rather than flight conditions. The minimum critical Reynolds numbers found by Mack at $M_e=4{\cdot}8$ for first and second modes are about 400 and 200 respectively at wave numbers of about 0·06 and 0·2 respectively. Mack's length scale is $\bar{L}=\sqrt{(\bar{\nu}_e\bar{x}/\bar{u}_e)}$. At $M_e\approx 5$ the boundary layer displacement thickness $\bar{\delta}$ is approximately $10\bar{L}$. Hence the values of wave number α and displacement thickness Reynolds number Re_δ reported below are roughly 10 times their respective 'Mack' values.

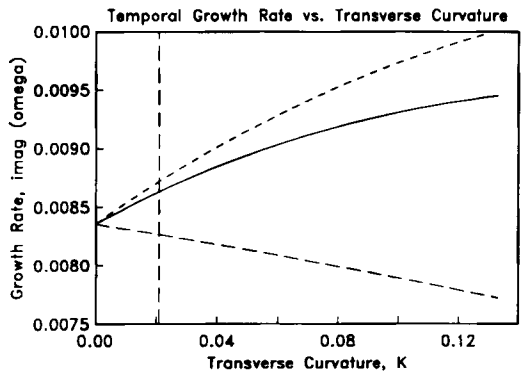

Figure 13. Variation in temporal growth rate of an asymmetric first-mode instability were subject to increasing transverse curvature: ——, combined effect; – – –, indirect effect; - - -, direct effect

Consider then the axisymmetric 'second-mode' instability whose parameter values are given by

$$\alpha = 2{\cdot}1, \qquad \beta = 0, \qquad Re_{\bar{\delta}} = 11\,000, \qquad R \gg 1 \tag{61}$$

and whose eigenvalue ω is identified by the point at $K = 0$ in Figure 10. The three curves for $K > 0$ describe the direct, indirect and combined influences on the eigenvalue ω when transverse curvature K is increased as all other parameters remain fixed. To assess the combined influence, the stability code is 'fed' a value of K and mean flow velocity and temperature profiles corresponding to the given curvature. The 'indirect effect' curve mimics the approximation of Mack,[16] in which curvature is accounted for in the mean flow profiles but curvature terms are neglected in the stability equations. The remaining possibility is represented by the 'direct effect' curve, for which curvature terms are modelled in the stability equations but the mean flow is that of a 'flat plate' ($K = 0$) boundary layer. The vertical line in Figure 10 marks the value of K which corresponds to $Re_{\bar{\delta}} = 11\,000$ for the Re given in (56). That stability is 'indirectly' quite sensitive to changes in the mean can be inferred by comparing the two velocity profiles of Figure 11 with the 'indirect effect" curve in Figure 10. Insight into the stabilizing trend is provided in Figure 12, which compares the variation of growth rate ω_i with wave number α for axisymmetric instability modes. The solid line defines the 'flat plate' ($K = 0$) case whereas the broken line corresponds to the 'combined effect' produced by a curvature value $K = 0{\cdot}0815$. As observed by Malik and Spall,[7] the second-mode hump is both diminished in height and shifted towards higher frequencies (higher wave numbers in temporal theory). Owing to the displacement, wave numbers on the long-wavelength (low-wave-number) side of the hump are strongly stabilized by increasing curvature.

Information similar to that found in Figure 10 is presented in Figure 13 for an asymmetric 'first-mode' instability wave whose parameter values are given by

$$\alpha = 0{\cdot}6, \qquad \beta = 1, \qquad Re_{\bar{\delta}} = 11\,000. \tag{62}$$

Here the obliqueness angle of 59° is near that which gives the greatest growth of Mach 5. In contrast to the previous case, the trend is toward destabilization with increasing curvature K. In comparing Figures 10, 12 and 13, it is interesting to note that the 'direct' and 'indirect' influences can tend in the same direction, as they do for the second-mode disturbance, or in opposite directions, as they do for the first mode. Our experience based on a limited number of cases is that

frequency ω_r is relatively insensitive to the effects of moderate curvature for the temporal model of stability.

Obviously, the influences of transverse curvature on primary instability mechanisms are subtle and further research is warranted. One conclusion, however, seems clear: whereas the effects of transverse curvature on compressible stability may be unimportant in many aerodynamic applications, it is ill-advised to ignore them routinely.

CONCLUSIONS

An efficient and highly accurate algorithm has been developed for numerical solution of the two-dimensional or axisymmetric compressible boundary layer equations and has been applied to a practical problem arising in compressible linear stability theory.

The numerical method incorporates a fifth-order, fully implicit, finite difference technique in the marching (streamwise) dimension and a spectral collocation technique using Chebyshev polynomials in the wall-normal dimension. Preconditioned Richardson iteration based on finite difference approximations of the Jacobian is used to minimize the residuals of the discrete governing equations at each marching step. The algorithm is shown to provide high-accuracy solution of the boundary layer equations with significantly fewer grid points than are required by standard finite difference methods. Execution time on a Cray YMP is less than 1 CPU second per marching step for a mesh of $N=77$ collocation points. The preconditioned iteration is computationally intensive in the sense that approximately 30 iterations are required to reduce the maximum residual by seven orders of magnitude. There are many possible preconditioning schemes, and refinement of the preconditioned iteration could likely improve global efficiency by as much as a factor of five.

A practical application of the algorithm arises in compressible linear stability theory, in the investigation of the effects of transverse curvature on the stability of flows over axisymmetric bodies. Curvature influences instability both directly, through the 'curvature terms' of the equations governing stability, and indirectly, through modification of the underlying mean flow. In particular, regarding the 'indirect' influence, transverse curvature destroys self-similarity of the boundary layer. Here we have used the spectral collocation algorithm to derive the non-similar mean velocity and temperature profiles in the boundary layer of a cylinder in a high-speed flow parallel to its axis. These profiles have subsequently been used as input to a spectrally accurate (temporal) stability code in order to assess both the direct and indirect effects of transverse curvature on stability. Although the streamwise variations in the mean are relatively small for Reynolds numbers typical of flight conditions, the stability of the flow is quite sensitive to these changes. Moreover, the direct and indirect influences can be additive or subtractive depending on the parameters of the flow and the wave numbers of the imposed disturbances. Because of the multiplicity of parameters and the many possible scenarios, further research is warranted. Whereas it may be possible in many aerodynamic applications to ignore the effects of transverse curvature on primary instability mechanisms, to do so routinely is ill-advised.

Perhaps a more significant question for transition researchers, and one that needs to be addressed, is how transverse curvature affects mechanisms of secondary instability.

ACKNOWLEDGEMENTS

The authors wish to express appreciation to Drs Peter Duck, Julius Harris, Venkit Iyer, Michele Macaraeg and Tom Zang for insights, suggestions and/or computer codes which contributed to

this work. The first author is grateful to the National Research Council for the associateship by means of which this work was conducted.

REFERENCES

1. F. G. Blottner, 'Computational techniques for boundary layers', *AGARD Lecture Series 73, Computational Methods for Inviscid and Viscous Two- and Three-Dimensional Flow Fields*, Von Karman Institute, 17–22 February 1975, pp. 3-1–3-51.
2. F. G. Blottner, 'Introduction to computational techniques for boundary layers', *Sandia National Laboratories Report SAND79-0893*, 1981.
3. J. E. Harris and D. K. Blanchard, 'Computer Program for solving laminar, transitional, or turbulent compressible boundary-layer equations for two-dimensional and axisymmetric flow', *NASA TM 83207*, 1982.
4. S. F. Wornom, 'Critical study of higher order numerical methods for solving the boundary-layer equations', *NASA TP 1302*, 1978.
5. C. L. Streett, T. A. Zang and M. Y. Hussaini, 'Spectral methods for solution of the boundary-layer equations', *AIAA Paper 84-1070, AIAA 22nd Aerospace Sciences Meeting*, Reno, NV, January 1984.
6. S. A. Orszag, 'Spectral methods for problems in complex geometries' *J. Comput. Phys.*, **37**, 70–92 (1980).
7. M. R. Malik and R. E. Spall, 'On the stability of compressible flow past axisymmetric bodies', *High Technology Report HTC-8905*, 1989.
8. H. Schlichting, *Boundary Layer Theory*, McGraw-Hill, New York, 1979, pp. 327–377.
9. F. M. White, *Viscous Fluid Flow*, McGraw-Hill, New York, 1974, pp. 576–624.
10. P. W. Duck, 'The inviscid axisymmetric stability of the supersonic flow along a cylinder', *ICASE Report 89-19 (NASA CR 181816)*, 1989.
11. NASA Ames Research Staff, 'Equations, tables, and charts for compressible flow', *NASA TR 1135*, 1965.
12. T. A. Zang, C. L. Streett and M. Y. Hussaini, 'Spectral methods for CFD', *ICASE Report 89-13 (NASA CR 181803)*, 1989.
13. C. Canuto, M. Y. Hussaini, A. Quarteroni and T. A. Zang, *Spectral Methods in Fluid Dynamics*, Springer, New York, 1988.
14. M. R. Malik, T. A. Zang and M. Y. Hussaini, 'A spectral collocation method for the Navier–Stokes equations', *J. Comput. Phys.*, **61**, 64–88 (1985).
15. L. M. Mack, 'Boundary-layer linear stability theory', in R. Michel (ed.), *Special Course on Stability and Transition of Laminar Flow, AGARD Report 709*, 1984, pp. 3-1–3-81.
16. L. M. Mack, 'Stability of axisymmetric boundary layers on sharp cones at hypersonic Mach numbers', *AIAA Paper 87-1413, AIAA 19th Fluid Dynamics, Plasma Dynamics and Lasers Conf.*, Honolulu, HI, June 1987.
17. K.-H. Kao and C.-Y. Chow, 'Stability analyses of boundary layer on a semi-infinite circular cylinder with and without spin', *AIAA Paper 90-0116, 28th Aerospace Sciences Meeting*, Reno, NV, January 1990.
18. K.-H. Kao and C.-Y. Chow, 'Stability of boundary layer on a blunt-nosed cylinder with and without spin', *AIAA Paper 90-0117, 28th Aerospace Sciences Meeting*, Reno, NV, January 1990.
19. M. G. Macaraeg, C. L. Streett and M. Y. Hussaini, 'A spectral collocation solution to the compressible stability eigenvalue problem', *NASA TP 2858*, 1988.